Erciyes Üniversitesi
Fen Bilimleri Enstitüsü Dergisi
Cilt 38, Sayı 2 , 2022

Erciyes University
Journal of Institue Of Science and Technology
Volume 38, Issue 2, 2022

Evolutionary Image Resizing based Accuracy Optimization for Aerial Triangulation

Hacı Mustafa PALANCIOĞLU, PhD.

Melikgazi Municipality, 38030, Kayseri City, Turkey, hacimustafapalancioglu@gmail.com

(Alınış / Received: 31.05.2022, Kabul / Accepted: 26.07.2022, Online Yayınlanma / Published Online: 23.08.2022)

Keywords
Aerial-imaging,
Multiscale DTM,
Image Downsampling,
Spatial Accuracy,
SfM Photogrammetry

Abstract: Flight altitude and properties of the imaging-sensor influence spatial-resolution of aerial-images used for SfM photogrammetry. Most mini-UAVs developed for civilian use can provide 8-bit, 12-64 MP RGB aerial images with geotags. As the number of aerial images obtained from related UAVs increases, various computational difficulties are encountered due to practical reasons for photogrammetric aerial triangulation process. Image Resizing is a common operation in SfM Photogrammetry for downsampling the aerial images. By using Image Resizing methods, images that are downsampled to different levels can make it easier to produce data that meets the desired accuracy criteria from aerial mapping. The high-frequency data is partially suppressed by softening the relevant image before it is reduced in order to prevent an excessive loss of detail in the image created after the Image Resizing process. Details may be lost, altered, or distorted as a result of excessive high-frequency data suppression or image smoothing. Therefore, it is difficult to implement the Image Resizing operation in an ideal way. In this paper, Bilateral Filter is used to smooth the related aerial images for Image Resizing. The best values of the internal parameters of the respective Bilateral Filter were calculated using the Differential Evolution Algorithm, DE. The statistical spatial-accuracy values computed for the photogrammetric products obtained by using resized images with DE-based Bilateral Filter exposed that the related products can met the spatial-accuracy standards for various engineering applications.

Havai Nirengi için Evrimsel Görüntü Yeniden Boyutlandırma Tabanlı Doğruluk En-İyileme

Anahtar Kelimeler
Havadan Görüntüleme,
Çok Ölçekli DTM,
Görüntü Alt-Örnekleme,
Uzamsal Doğruluk,
SfM Fotogrametrisi

Öz: Uçuş yüksekliği ve görüntüleme sensörünün özellikleri, SfM fotogrametrisi için kullanılan hava görüntülerinin uzamsal çözünürlüğünü etkiler. Sivil kullanım için geliştirilen mini İHA'ların çoğu, GNSS-tabanlı coğrafi etiketli 8 bit, 12-64 MP RGB hava görüntüleri sağlamaktadır. İlgili İHA'lardan elde edilen hava görüntülerinin sayısı arttıkça, fotogrametrik hava nirengi işlemi için pratik nedenlerden dolayı çeşitli hesaplama güçlükleri ile karşılaşılır. Görüntü Yeniden Boyutlandırma, SfM Fotogrametrisinde havadan görüntülerin alt-örneklenmesi için kullanımı gerekli olan yaygın bir işlemdir. Görüntü Yeniden Boyutlandırma yöntemleri kullanılarak, farklı düzeylerde alt-örneklenen görüntüler, havadan haritalamada istenen doğruluk kriterlerini karşılayan verilerin üretilmesini kolaylaştırabilir. Görüntü Yeniden Boyutlandırma işlemi sonunda üretilen görüntüde aşırı detay kaybına neden olmamak için yüksek frekanslı veriler, görüntü küçültülme işleminden önce kısmen bastırılır. Görüntünün aşırı yumuşatılması veya yüksek frekanslı verilerin aşırı bastırılması, ayrıntıların değişmesine, bozulmasına veya kaybolmasına neden olabilir. Bu nedenle, Görüntü Yeniden Boyutlandırma işlemini ideal bir şekilde uygulamak zordur. Bu makalede, Görüntü Yeniden Boyutlandırma için ilgili hava görüntülerini yumuşatmak amacıyla ikili bir filtre yapısı kullanılmıştır. İlgili İkili Filtrenin dahili parametrelerinin en iyi değerleri, Diferansiyel Evrim Algoritması, DE kullanılarak hesaplanmıştır. DE tabanlı İkili Filtre, yani Bilateral Filtre, ile yeniden boyutlandırılmış görüntüler kullanılarak elde edilen fotogrametrik ürünler için hesaplanan istatistiksel mekansal doğruluk değerleri, ilgili ürünlerin çeşitli mühendislik uygulamaları için mekansal doğruluk standartlarını karşılayabileceğini ortaya koymuştur.

---

*Corresponding Author, email: hacimustafapalancioglu@gmail.com

1. Introduction

An estimation of three-dimensional structures from two-dimensional image sequences containing local motion data is called Structure from Motion (SfM) Photogrammetry [1-2]. Numerous image processing applications use various image resampling/resizing techniques, including SfM, video rescaling, image/video transmission, pansharpening, image fusion, and multi sensor medical imaging [3-6]. The band-width of image transmission and the run-time cost of image processing tasks dramatically grows up with increasing size of image and inherent complexities of algorithms used for image processing. To keep the efficiency of the image processing process within acceptable time and computational cost limitations, some detail-preserving image resampling / resizing methods [7-10] and parallel-image processing methods must be utilized.

In the process of applying non-recursive image processing operators to the related aerial-image, parallel-image processing methods [11-12] and hardware are frequently utilized in photogrammetry. GPUs, which offer analytical and practical advantages, are the most crucial piece of parallel image processing hardware in SfM photogrammetry-based image processing applications. The most recent photogrammetric data processing software uses C-based CUDA architectures and software development toolboxes to make practical use of GPUs. GPUs are used to solve optimization issues in image matching, ray tracing, photogrammetric resection/intersection, and various bundle block modification methods. Advanced imaging sensors enable the capture of images with a higher spatial resolution [13-15] but a larger number of pixels to process. Computational complexity, data processing capacity, and run-time are all reasonable restrictions for CPUs and GPUs. Therefore, optimizing image frequency and resolution of the aerial images have an important effect on run-time of data processing, overall-accuracy and cost of photogrammetric end-products, such as Digital Terrain Model (DTM) [16-18], Point Cloud [19] and Ortophoto [20].

A point cloud is basically a collection of data points in a three-dimensional coordinate system, typically defined by the x, y, and z coordinates of the physical entity being measured. Photogrammetry is an indirect method used to capture 3D point clouds, in contrary to Lidar technology [21-22].

The Ground Sample Distance (GSD) [23] value refers to the spatial resolution of an image and indicates the size at which a pixel's dimensions correspond in the physical scene. If the spatial accuracy [24-27] values expected from the photogrammetric result products are much larger than the average GSD value of the photogrammetric image, various image downsampling methods can be used to efficiently use the run-time, cost and computational resources of the computational platform.

The two main factors that allow choosing detail information among image primatives are the presence of high contrast situations and the level of radiometric resolution. Therefore, the Nyquist frequency (also known as the folding frequency), which is equal to half of the original picture sampling frequency, should be used to govern the image downsampling process. It is possible to partially preserve edges and other high contrast features by avoiding aliasing artifacts in the edge regions.

The image interpolation technique employed in the downsampling process has several built-in characteristics that contribute to some of the low level artificial artifacts on the downsampled image. In other words, because it has the potential to change the technical quality of the relevant end products of photogrammetric goods, the picture resampling / interpolation method used in the downsampling process should be chosen for analytical reasons.

Artificial image blocking, random valued additive noise, speckle noise, thermal noise, gaussian noise, and dynamic local-intensity turbulence effects have all been successfully suppressed using various image filtering methods. Image enhancement filters with dominant detail retention qualities, such as the Center-Weighted Mean Filter, Nonlocal Mean Filter [28], and Bilateral Filter [29], are used to improve the efficiency of image processing procedures in photogrammetric images. Therefore, the image enhancement filter should be selected according to balance between runtime complexity and the a few factors that effects the detail preserving ability of SfM tasks used.

In general, SfM photogrammetry data sets are organised as big-data sets that have large numbers of aerial images. Therefore, using properly planned image downsampling procedures to efficiently complete SfM photogrammetry calculation processes with restricted resources is particularly valuable in SfM photogrammetry. In this paper, the aerial images have been captured by using a modified DJI Phantom 4 Pro that it has been equipped with post-process kinematic GNSS (PPK) based image geotagging hardware [30]. PPK geotagging [31] is based on the use of a GNSS PPK receiver that is also capable of time-stamp based driving the drone's camera. This solution does not require the drone and ground base station to communicate with one another. Unlike the real-time positioning (RTK) approach [32-34], the precision of the observation data recorded onto onboard PPK receiver is enhanced by processing the base station data in conjunction with the reference GNSS observation station data off-line. In comparison to PPK RTK, it is less susceptible to communication failures. Reference observations of PPK computations have been supplied from Tusaga Aktif Network and an indirect automatic aerial triangulation phase has been used in photogrammetric computations.

The following are the contributions of the results reported in this paper to 3D image processing community:

1. The generalization and information smoothing impact of aerial image size on the accuracy of photogrammetric point clouds have been thoroughly investigated.

2. A new image downsampling method able to preserve chromatic information and image-features has been presented.

3. The relative spatial accuracies of point clouds based on downsampled images has been investigated by using M3C2 metric.

4. The effects of image downsampling on run-time complexity of photogrammetric data processing tasks has been analysed.

5. Using point cloud dilution techniques, multiscale digital surface models create oversimplified representations of the observed landscape. The creation of smoothed digital models of the environment via point cloud synthesis based on picture downsampling is far too practicable. This study investigates how image downsampling affects point clouds' ability to carry spatial detail.

This paper has been organized as follows: In Section 2, Method is given. In Section 3, Image Downsampling with Detail-Preserving is presented. Experiments given in Section 4 and Section Results and Conclusions presented in Section 5.

2. Method

Because of its capacity to map the environment quickly and inexpensively, SfM photogrammetry is an active research area in *computer vision* and *3D computational perception*. SfM is the ability of humans (and other living animals) to reconstruct 3D structure from a projected 2D motion field of a moving object or scene. Due to automated procedures in recently developed SfM photogrammetric software, SfM photogrammetry has become a too practical 3D measurement technique. Thanks to characteristics of SfM, vision based 3D environment mapping has become much easier. Scattered and coloured *point clouds* are main data sources of multiscale 3D mesh forms of virtual environment maps. In recent years, automation in SfM photogrammetry tasks has been increased to facilitate the coloured *point clouds* generation procedures. Lots of SfM photogrammetry software have the ability of automatic *image matching / alignment*, *point cloud generation*, *texture synthesis* and *virtual model reconstruction* tasks. Even while commercial software is stronger in 3D modelling, some of the *freeware* and *open-source* SfM software have many features to accurately and detailly mapping the environment. Table 1 lists some frequently used SfM photogrammetry and point cloud processing tools.

Spatial resolution of an aerial image is usually given in *Ground Sample Distance* (GSD) [23]. The detail detection ability of image processing tasks becomes easier as GSD increases. The time required to compute aerial triangulation increases with pixel count. Downsampling results in a higher GSD and partially loss of image detail. The amount of time and system resources required to complete SfM computations is decreased by image downsampling, resulting in increased efficiency. To lower the *spatial frequency* or *spatial resolution* of a $[M \times N]$ pixels-sized image, one of two image downsampling method is usually employed. The first method is based on sampling in a *uniform* manner. This strategy can lead to appear *image blur*, *aliasing effects*, and *artificial-edges* on the downsampled images at different rates. Non-uniform sampling is the second method used to image downsampling. The downsampled images generated by this strategy have a relatively improved detail preservation capacity, and downsampled images are less impacted by blurring and aliasing effects.

Fig. 1 illustrates how image downsampling effects the image details for the downsampling rates employed in the Experiments.

Table 1 : Tools for SfM Photogrammetry.

#	Software name	Web Address	Functionality
1	APS Menci	https://www.mencisoftware.com/	SfM Photogrammetry
2	AutoDesk ReCap Photo	https://www.autodesk.com/products/recap	SfM Photogrammetry
3	Colmap	https://colmap.github.io/	SfM Photogrammetry
4	Correlator3D	https://www.simactive.com/	SfM Photogrammetry
5	Drone2Map	https://www.esri.com/	SfM Photogrammetry
6	DroneDeploy	https://www.dronedeploy.com/	SfM Photogrammetry
7	DroneMapper	https://dronemapper.com/	SfM Photogrammetry
8	Globalmapper	https://www.bluemarblegeo.com/global-mapper/	SfM Photogrammetry
9	Meshroom	https://github.com/alicevision/meshroom/releases	SfM Photogrammetry
10	Metashape	https://www.agisoft.com/	SfM Photogrammetry
11	MicMac	https://micmac.ensg.eu/index.php/Accueil	SfM Photogrammetry
12	Open Drone Mapping	https://www.opendronemap.org/	SfM Photogrammetry
13	Photomodeler	https://www.photomodeler.com/	SfM Photogrammetry
14	Pix4Dmapper	https://www.pix4d.com	SfM Photogrammetry
15	PrecisionMapper	https://www.precisionmidwest.com/	SfM Photogrammetry
16	Reality Capture	https://www.capturingreality.com/	SfM Photogrammetry
17	Regard3D	https://www.regard3d.org/	SfM Photogrammetry
18	VisualSFM	http://ccwu.me/vsfm/	SfM Photogrammetry
19	3DR Zephyr	https://www.3dflow.net/	SfM Photogrammetry
20	Meshlab	https://www.meshlab.net/	Data Processing, CAD
21	Autodesk Revit	https://www.autodesk.com.tr/	Data Processing, CAD
22	CloudCompare	https://www.danielgm.net/cc/	Data Processing, CAD
23	VRMesh	https://www.vrmesh.com/	Data Processing, CAD
24	PointTools	https://www.bentley.com/	Data Processing, CAD
25	VirtualSurvey	https://www.virtual-surveyor.com/	Data Processing, CAD

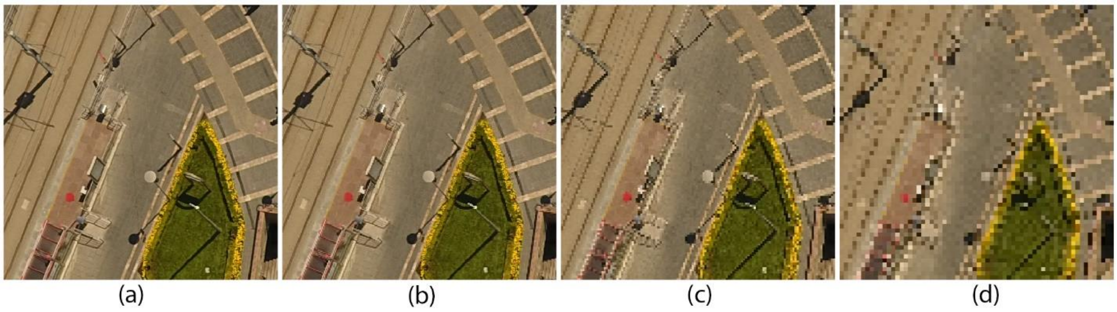
(a) (b) (c) (d)

Figure 1 : The effect of downsampling on 8-bit RGB images with the size of [512x512] pixels : (a) Original, (b) $\frac{1}{2}$ downsampled, (c) $\frac{1}{4}$ downsampled, (d) $\frac{1}{8}$ downsampled.

Fig. 2 illustrates how SfM photogrammetry works.

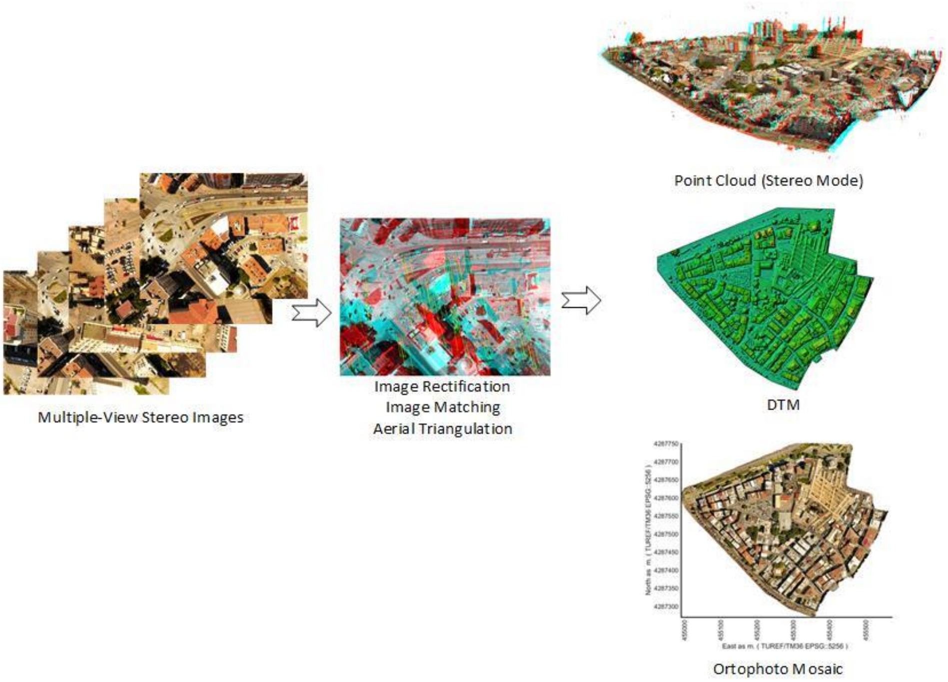

Figure 2 : Steps of SfM Photogrammetry.

Aliasing can be prevented by pre-filtering the image using a smoothing filter prior to image downsampling. Bilateral filter [29,35] is a non-linear image smoothing filter that supresses noise. It substitutes the intensity of each pixel with a *gaussian* weighted average of surrounding pixels. The weights take into account not just pixel distance but also radiometric discrepancies. Bilateral filter has been defined in Eq. 1.

$$I_{filtered}(x) = \frac{1}{W_p}\sum_{x_i \in \Omega} I(x_i) \cdot f_r(\|I(x_i) - I(x)\|) \cdot g_s(\|x_i - x\|) \quad (1)$$

where $W_p = f_r(\|I(x_i) - I(x)\|) \cdot g_s(\|x_i - x\|)$. Here, $I_{filtered}, I, x, \Omega$ denotes filtered image, original image, spatial coordinates of current pixel to be filtered, and window centred at x, respectively. $x_i \in \{\Omega \backslash x\}$. f_r, g_s represent range kernel for smoothing intensity differences and spatial kernel for smoothing coordinate disparities. The spatial proximity and intensity difference are used to compute the value of W_p. To smooth image pixels, a Bilateral filter employs the *gaussian* range and *spatial kernel*s defined in Eq. 2.

$$w(i,j,k,l) = e^{\left(-\frac{(i-k)^2+(j-l)^2}{2\sigma_d^2} - \frac{\|I^2 - I(k,l)^2\|}{2\sigma_r^2}\right)} \quad (2)$$

where σ_d, σ_r are smoothing parameters of Bilateral filter. $I(i,j)$, and $I(k,l)$ denotes the pixel intensities of (i,j), and (k,l). The weights are normalized by using Eq. 3 ;

$$I_D(i,j) = \frac{\sum_{k,l} I(k,l) \cdot w(i,j,k,l)}{\sum_{k,l} w(i,j,k,l)} \quad (3)$$

where I_D is the denoised intensity of pixel (i,j). With increasing range parameter σ_r, the bilateral filter approaches *gaussian* convolution more closely because the range *gaussian* expands and flattens, becoming virtually constant across the image's intensity interval. Larger features are smoothed as σ_d rises.

In this paper, the optimized values of σ_r and σ_d have been computed by using *Differential Evolution Algorithm* (DE or DE/rand/1/bin) [36]. DE is an evolutionary computing based, non-recursive optimization method. Despite its simplicity, it solves most optimization issues. DE is a library of 6 mutations and 2 crossover operators. The most commonly used DE is *DE/rand/1/bin*. In this paper, *DE/rand/1/bin* has been used to solve the equation in Eq. 4 to compute the optimal values of $(\sigma_r, \sigma_d, win)$. A DE structure based on binomial crossover was employed in this paper. The fusion of three different vectors serves as the foundation for the DE's mutation operator. By manually adding the scaled form of the direction vector that is obtained by calculating the difference between the first two vectors to the third vector, the related fusion process is completed.

The $MaxIteration$=10000, CR=0.50, and $F=\frac{(\lambda-0.50)}{0.50}|\lambda \sim U(0,1)$ have been used to setting of the inherent parameters of *DE/rand/1/bin* seen in Fig. 3. Readers can find more detailed information on *DE/rand/1/bin* algorithm defined in Fig. 3 at [36].

Original aerial images have been captured as *.jpeg images with [3000x4000] pixels in size with 8-bit RGB colour space. To conserve *colormatic information*, all RGB images have been transformed to CIE L*a*b colour space before applying the Bilateral filter to related images.

The objective function used to calculate the optimized values of $\sigma_r$and σ_d is defined in Eq. 4;

$$\underbrace{argmin}_{\sigma_r,\sigma_d,win} -\frac{1}{NI}\sum_{l=1}^{NI} ssim\left(upsample(I_D^{(\sigma_r,\sigma_d,w)}, I_l); I_l\right) \tag{4}$$

where $upsample(I_D^{(\sigma_r,\sigma_d,win)}, I)$ infers upsampled image of $I_D^{(\sigma_r,\sigma_d,win)}$ to the size of original image, $I_{l=\{1:NI\}}$. Here, $I_D^{(\sigma_r,\sigma_d,win)}|I_D^{(\sigma_r,\sigma_d,win)} = downsample(I^*)$ denotes downsampled image of I^*, where $I^* = BilateralFilter(I, \sigma_r, \sigma_d, win)$. win denotes *sliding window* size used by Bilateral filter. Presented method in Eq. 4 significantly preserves the edge features and chromatic information during image downsampling process.

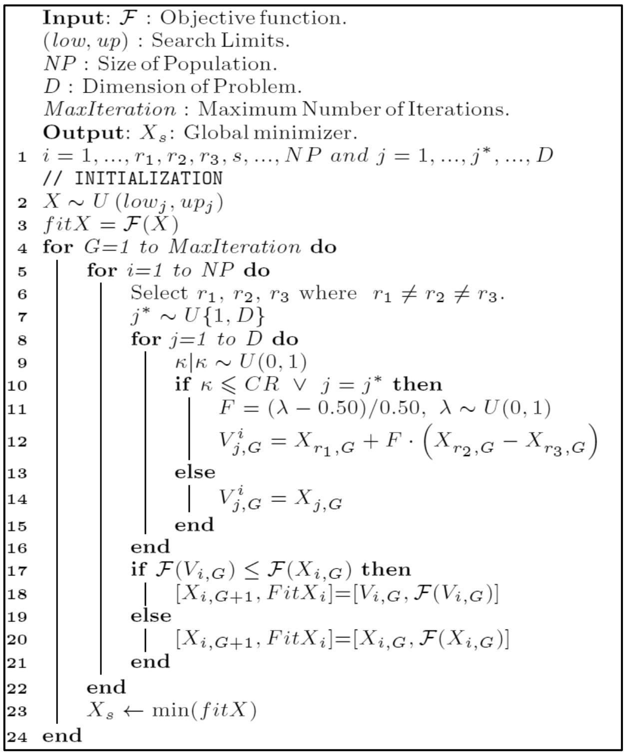

```
Input: $\mathcal{F}$ : Objective function.
       $(low, up)$ : Search Limits.
       $NP$ : Size of Population.
       $D$ : Dimension of Problem.
       $MaxIteration$ : Maximum Number of Iterations.
Output: $X_s$: Global minimizer.
$i = 1, ..., r_1, r_2, r_3, s, ..., NP \; and \; j = 1, ..., j^*, ..., D$
// INITIALIZATION
$X \sim U(low_j, up_j)$
$fitX = \mathcal{F}(X)$
for $G$=1 to $MaxIteration$ do
    for $i$=1 to $NP$ do
        Select $r_1$, $r_2$, $r_3$ where $r_1 \neq r_2 \neq r_3$.
        $j^* \sim U\{1, D\}$
        for $j$=1 to $D$ do
            $\kappa|\kappa \sim U(0,1)$
            if $\kappa \leqslant CR \vee j = j^*$ then
                $F = (\lambda - 0.50)/0.50, \; \lambda \sim U(0,1)$
                $V_{j,G}^i = X_{r_1,G} + F \cdot \left(X_{r_2,G} - X_{r_3,G}\right)$
            else
                $V_{j,G}^i = X_{j,G}$
            end
        end
        if $\mathcal{F}(V_{i,G}) \leq \mathcal{F}(X_{i,G})$ then
            $[X_{i,G+1}, FitX_i]$=$[V_{i,G}, \mathcal{F}(V_{i,G})]$
        else
            $[X_{i,G+1}, FitX_i]$=$[X_{i,G}, \mathcal{F}(X_{i,G})]$
        end
    end
    $X_s \leftarrow \min(fitX)$
end
```

Figure 3 : DE (DE/rand/1/bin) algorithm [36].

The $ssim(img, refimg)$ function used in Eq. 4 denotes *Structural Similarity Index* [37] defined by using Eq. 5 as;

$$ssim(img; refimg) = \frac{(2\mu_{img}\mu_{refimg}+c_1)(2\sigma_{img;refimg}+c_2)}{(\mu_{img}^2+\mu_{refimg}^2+c_1)(\sigma_{img}^2+\sigma_{refimg}^2+c_2)} \tag{5}$$

where μ_x, μ_y denotes average of img, and $refimg$, respectively. σ_{img}^2, σ_{refimg}^2, and $\sigma_{img;refimg}$ denotes variance of img, $refimg$ and covariance of img and $refimg$.

Fig. 4 illustrates the computation procedure of Eq. 4.

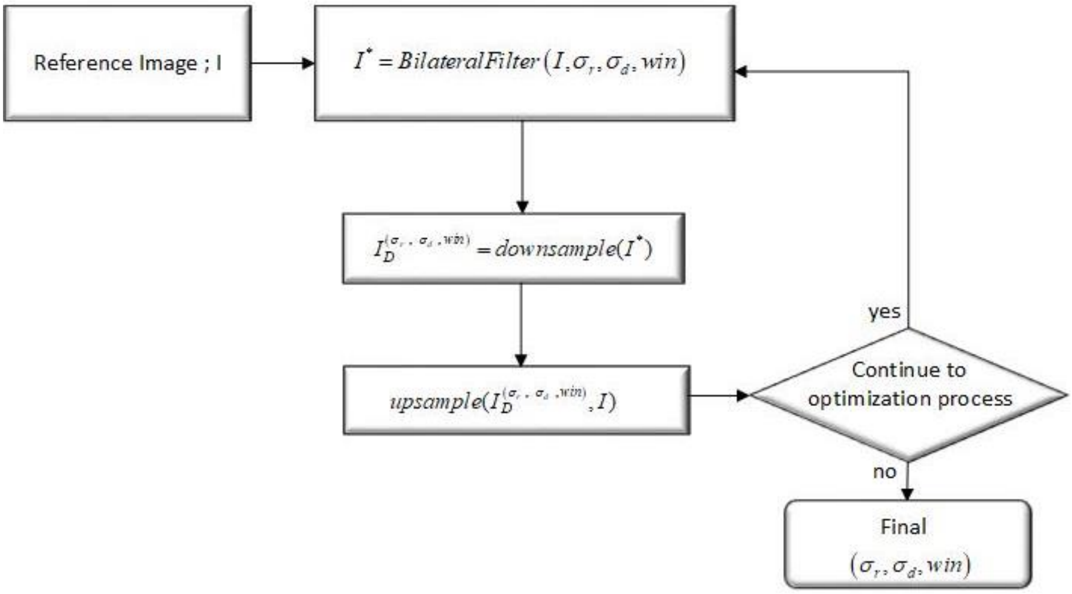

Figure 4 : The flowchart of computation steps of objective function, Eq. 4, used for image downsampling.

All of the aerial images have been downsampled together by using the procedure defined in Eq. 4. The optimized values of the parameters of the Bilateral filter are listed in Table 2 for the each downsampling rate.

The *search space* limits of σ_r and σ_d have been set to $[low; up]_{\sigma_r and \sigma_d} = [0; 100]$ and the *search space* limits of win has been set to $[low; up]_{win} = \{3; 11\}$, where $win \in \{3,5,7,9,11\}$ for *DE/rand/1/bin* based raw-genetic optimization phase (see Fig. 3, line 2 for $[low; up]$).

Table 2 : The optimized values of the parameters of the Bilateral filter by using DE for related downsampling rates.

Downsampling Rate	Numeric value of Eq. 2	Parameters of the Bilateral filter (*see* Eq 2 *for* σ_r *and* σ_d)		
		σ_r	σ_d	win
1/2	0.96986	0.5647	48.2994	3
1/4	0.92904	0.0176	83.1680	3
1/8	0.89079	1.0696	71.0628	3

The Bilinear Interpolation method [38] has been used for image resizing [39-45] operations related with Eq 4, due to its high *colormatic information preserving* capacity [46] of resized image [47,48].

4. Experiments

The aerial images utilized in the experiments were obtained using a small-scale photogrammetric flight mission conducted with a drone. To geotag images, a modified DJI Phantom Pro 4 drone with post-process kinematic (PPK) positioning capability has been utilized. Image were captured as 8-bit, 12MP RGB images with 3000x4000 pixels in size. The photogrammetric flying mission was planned and executed using DroneDeploy autopilot software on an iOS device [49].

Figure 5 : The modified PPK based UAV platform used to acquire photogrammetric aerial-images used in the Experiments.

The photogrammetric *Front* and *Side Overlap* values [50, 51] have been set to 80%, and 75%, respectively. *Mapping Flight Speed* value has been set to 8m/s, which is enough to avoid *motion blur* in captured images. The *Flight Altitude*=120 m., *Focal Length*= 8.6 mm, Imaging *Sensor Width*=12.8333 mm, and GSD=4.48 cm/pixels values have been used to apply photogrammetric flying mission. The GSD of acquired images are [179.20 x 134.40] m. in [width x high] of related images.

The *Test Field* has been centred at $Latitude = 38^0.719736$, $Longitude = 35^0.485746$ in Kayseri City, Turkish Republic. The area of the *Test Field* is 162471.35 m^2 or 40.147 acres. The point clouds generated by using the downsampled aerial images have been labelled as $Data\#1$, $Data\#2$,$Data\#3$, and $Data\#4$, respectively. The point clouds of $Data\#1$, $Data\#2$,$Data\#3$, and $Data\#4$ have been generated by using the image data sets with the size of pixels 3000×4000 (i.e., original images), 1500×2000 (i.e., $\frac{1}{2}$ downsampled-images), 750×1000 (i.e., $\frac{1}{4}$ downsampled-images), and 375×500 (i.e., $\frac{1}{8}$ downsampled-images), respectively.

Each of the image data sets were processed separately by using the freeware SfM software, *Meshroom* [52], and the generated dense point cloud has been exported as point cloud file. The related point cloud files have been used in piecewise point cloud comparison analysis by using the *Multiscale Model-to-Model Cloud Comparison*, M3C2 [53], function of freeware point cloud processing software, *CloudCompare* [54].

M3C2 was created to facilitate the comparison of point clouds on complex surfaces. The first phase of M3C2 is to compute the local-point *normal directions* of each point in the reference point cloud using neighbours that are closer to the relevant point than the D distance. The second step calculates the M3C2 value for the Euclidean distance (i.e., l_2 norm) between the lower and upper surfaces of an artificial cylinder of height L and diameter d centred on the local normal direction determined in the first step. The reference and comparison point clouds are used to construct the *best-fit* planes representing the bottom and upper surfaces of the appropriate artificial cylinder. Fig. 6 illustrates the analytical concept behind M3C2 distance.

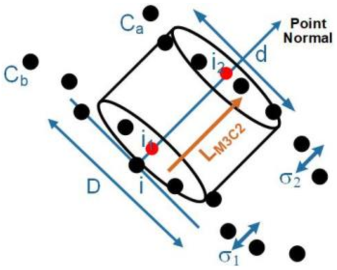

Figure 6 : Illustration of the analytical concept behind M3C2 distance.

The $d_{(1;2)}$, $d_{(1;3)}$,$d_{(1;4)}$,$d_{(2;3)}$,$d_{(2;4)}$ and $d_{(3;4)}$ denotes the computed $M3C2$ values between the point clouds of $(Data\#1; Data\#2)$, $(Data\#1; Data\#3)$, $(Data\#1; Data\#4)$, $(Data\#2; Data\#3)$, $(Data\#2; Data\#4)$, and $(Data\#3; Data\#4)$, respectively.

All of the computations realized by using a HP Z820 PC that have an intel(R) Xeon(R) CPU E5-2640 0 @ 2.50GHz 2.50, Win 10 Pro 64 bit OS, 64 Ram, and two GPU (i.e., Quadro K5000, Tesla K20c).

Some of the basic statistics of the empirical results of the numerical analysis have been tabulated at Table 3.

Table 3 : Basic statistics of the Experiments.

Features	Data#1	Data#2	Data#3	Data#4
Rate of image downsampling	1/1	1/2	1/4	1/8
Numbers of aerial images	105	105	105	105
Flying altitude (m)	120	120	120	120
Size of image orientation points (Tie-Points) (points)	369 824	368 840	333 377	98 046
Size of dense cloud (points)	294 781 104	74 406 689	18 006 229	4 535 837
Tie point density (points/m2)	2.28	2.27	2.05	0.60
Point cloud density (points/m2)	4 398.93	457.97	110.83	27.92
Image size (pixels)	3000x4000	1500x2000	750x1000	375x500
Ground Sample Distance (GSD) (cm)	3.27	6.54	13.08	26.16

Table 3 shows that the most significant effect of reducing *image resolution* is on GSD. GSD increases as image resolution decreases, as does the smallest identifiable object size limit value. This is significant since the *detail-mapping* capacity is too sensitive to image resolution. Similarly, when image resolution declines, topographic details expressed by DTM [55] are smoothed or dismissed. As a result, by removing some topographic characteristics, low-resolution aerial image-based mapping enables us to create multiscale DTM models. Data processing is facilitated by multiscale DTMs in return for the partial erasure of detail data. Therefore, multiscale DTM models are essential and too beneficial in several applications, including multimedia GIS, augmented and virtual reality, applications for narrow-band topographic data transmission, and augmented and virtual reality.

The generated ortophoto (i.e., map-like-image) of the *Test Area* for the $Data\#1$has been illustrated in Fig. 7.

There are 20 ground control points [56] homogeneously distributed over the *Test Area* have been used in the aerial triangulation. One GNSS receiver, Ashtech Promark 500, has been used both to measure spatial coordinates of the ground control points and to capture reference point observations for post-process kinematic, PPK, positioning. PPK computations have been achieved by using a modified version of the freeware PPK software, RTKLib [57]. The GNNSS sensor of NEO/LEA-M8T from U-BLOX [58] has been used to trigger the drone camera and related sensor captured high resolution time steps of image acquisition times with GNSS observation flows for PPK computations.

The Test Area, as depicted in the orthophoto that follows, is made up of a number of urban fields, each with its own geometrical characteristics, such as vegetation regions and flat or curved surfaces. By carefully interpreting the computed M3C2 values, researchers may be able to choose the spatial resolution of aerial images needed for a workable small-scale aerial mapping of urban areas.

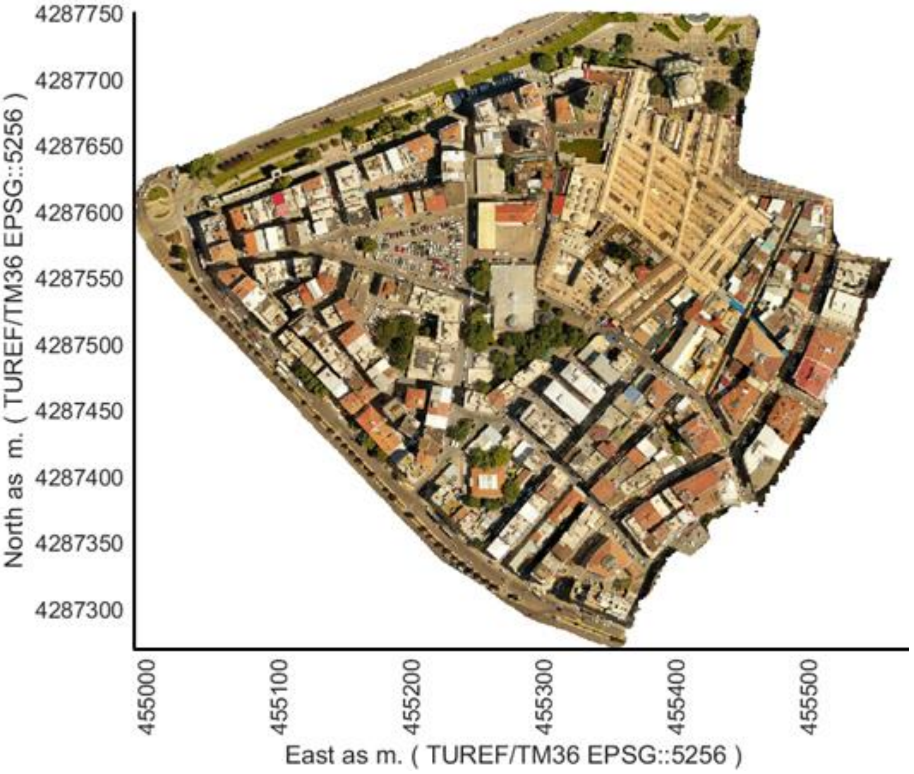

Figure 7 : Ortophoto of the *Test Area* (Grid-size 0.25x0.25m has been used for illustration).

The statistics of point cloud -to- point cloud comparison tests based on $M3C2$ values have been tabulated in Table 4. The Sample# denote number of 3D points remained within the related interval. The Sample%, denote the percentage ratio of related Sample# to summation of Sample# at same raw. The Csum denote cumulative summation value of Sample% values at same raw.

Table 4 : The statistics of point cloud -to- point cloud comparison tests based on $M3C2$ values.

$M3C2$	Statistics	Lower-Upper Limits of Binning Intervals for $M3C2$					
		0.00- 0.20 m.	0.20- 0.40 m.	0.40- 0.60 m.	0.60- 0.80 m.	0.80- 1.00 m.	1.00+ m.
d_{1_2}	Sample#	1 472 419	877 462	322 869	92 632	50 653	304 568
	Sample%	47.18	28.12	10.35	2.97	1.62	9.76
	Csum	47.18	75.3	85.65	88.62	90.24	100
d_{1_3}	Sample#	799 381	564 517	761 879	290 540	110 477	593 809
	Sample%	25.62	18.09	24.41	9.31	3.54	19.03
	Csum	25.62	43.71	68.12	77.43	80.97	100
d_{1_4}	Sample#	342 006	222 941	231 160	244 975	282 118	1 797 403
	Sample%	10.96	7.14	7.41	7.85	9.04	57.6
	Csum	10.96	18.1	25.51	33.36	42.4	100
d_{2_3}	Sample#	1 095 963	514 505	114 984	39 752	24 489	187 105
	Sample%	55.44	26.03	5.82	2.01	1.24	9.47
	Csum	55.44	81.47	87.29	89.3	90.54	100.00
d_{2_4}	Sample#	338 194	249 095	223 361	214 864	223 679	727 605
	Sample%	17.11	12.6	11.3	10.87	11.32	36.81
	Csum	17.11	29.71	41.01	51.88	63.2	100.00
d_{3_4}	Sample#	42 619	37 311	35 793	24 919	9 495	26 605
	Sample%	24.11	21.11	20.25	14.1	5.37	15.05
	Csum	24.11	45.22	65.47	79.57	84.94	100.00

The results obtained from the analysis of the d_{1_2} values shown in Table 4 are given below;

- ✓ 47.18% of Sample# values are less than 0.20 m. Relevant data are mostly observed in relatively horizontal areas such as flat building roofs, road sections with very low slopes.
- ✓ 28.12% of Sample# values are less than 0.40 m. Relevant data are mainly observed in areas where the local variation of the slope is relatively fast. In relatively flat areas, 73.30% of M3C2 values are less than 0.40 m.
- ✓ 10.35% of Sample# values are less than 0.60 m. Relevant data were observed mainly in green areas.
- ✓ 2.97% of Sample# values are less than 0.80 m. Relevant data have been observed intensively on vertical surfaces such as building exteriors.
- ✓ 1.62% of Sample# values are less than 1.00 m. Relevant data were observed in densely wooded areas.
- ✓ 9.76% of Sample# values are greater than 1.00 m. Relevant data were observed in densely wooded areas.

The results obtained from the analysis of the d_{1_3} values shown in Table 4 are given below;

(a) 25.62% of Sample# values are less than 0.20 m. Relevant data are mostly found in flat regions like roofs and road sections with very low slopes.
(b) 18.09% of Sample# values are less than 0.40 m. Relevant d_{1_3}values were generally observed on building roofs. Only 43.71% of M3C2 values are less than 0.40 m. for the d_{1_3}. This statistic demonstrates that when the image resolution lowers, the amplitude of the M3C2 values between the relevant point clouds increases. The primary reason for this is that point clouds generated from low quality photos have far less detail.
(c) 24.41% of Sample# values are less than 0.60 m. Relevant Sample# values are generally observed in flat areas.
(d) 9.31% of Sample# values are less than 0.80 m. Relevant Sample# values are generally observed in flat areas.
(e) 3.54% of Sample# values are less than 1.00 m. Relevant data were observed in densely wooded areas.
(f) 19.03% of Sample# values are greater than 1.00 m. Relevant data were observed in densely wooded areas and at a neglectable border section of test field.

The results obtained from the analysis of the d_{1_4} values shown in Table 3 are given below.

(a) 10.96% of Sample# values are less than 0.20 m. Relevant data are mostly found in flat regions like roofs and road sections with very low slopes.
(b) 7.14% of Sample# values are less than 0.40 m. Relevant d_{1_4} values were generally observed on building roofs. Only the 18.10% of M3C2 values of d_{1_4} are less than 0.40 m.
(c) 7.41% of Sample# values are less than 0.60 m. Relevant Sample# values are rarely observed in flat areas.
(d) 7.85% of Sample# values are less than 0.80 m. Relevant Sample# values are rarely observed in flat areas.
(e) 9.04% of Sample# values are less than 1.00 m. Relevant data were observed in densely all field types.
(f) 57.60% of Sample# values are greater than 1.00 m. Relevant data were observed in densely all field types. Due to the fact that $Data\#4$ is an overgeneralized point cloud, the majority of the d_{1_4} values have been piled in this range. $Data\#4$ enables for a more generic topographic structure to be defined, which may be used in multimedia applications, as well as a reduction in bandwidth for spatial data transfer.

The results obtained from the analysis of the d_{2_3} values shown in Table 4 are given below.

(a) 55.44% of Sample# values are less than 0.20 m. In and around buildings relatively far from the drone flight plane, this sort of data has been observed intensively.
(b) 26.03% of Sample# values are less than 0.40 m. This type of data has been noticed extensively in and around buildings that are somewhat close to the drone flight plane. The 81.47% of M3C2 values of d_{2_3} are less than 0.40 m.
(c) 5.82% of Sample# values are less than 0.60 m. Relevant Sample# values are rarely observed in flat areas.
(d) 2.01% of Sample# values are less than 0.80 m. Relevant Sample# values are rarely observed in flat areas.
(e) 1.24% of Sample# values are less than 1.00 m. Relevant data were observed in densely all field types.

(f) 9.47% of Sample# values are greater than 1.00 m. Relevant Sample# values are rarely observed in flat areas.

The results obtained from the analysis of the d_{2_4} values shown in Table 4 are given below.

(a) 17.11% of Sample# values are less than 0.20 m. This sort of data has been observed on surfaces that are somewhat distant from the flight plane.
(b) 12.60% of Sample# values are less than 0.40 m. This sort of data has been observed on surfaces that partially flat or are somewhat distant from the flight plane. The 81.47% of M3C2 values of d_{2_3} are less than 0.40 m.
(c) 11.30% of Sample# values are less than 0.60 m. Relevant Sample# values are rarely observed in flat areas.
(d) 10.87% of Sample# values are less than 0.80 m. Relevant Sample# values are rarely observed in flat areas.
(e) 11.32% of Sample# values are less than 1.00 m. Relevant data were observed in densely all field types.
(f) 36.81% of Sample# values are greater than 1.00 m. Relevant Sample# values are rarely observed in flat areas.

As image spatial resolution grows, the geographical distribution of M3C2 values becomes more uniform, however as image spatial resolution drops, the M3C2 values exhibit speckle / impulsive noise characteristics and become relatively visible across the *Test Area*. The primary reason for this is because the ability of point clouds to generalize related surfaces increases with the image downsampling rate. With increasing downsampling rate, details are eroded, the point cloud becomes more susceptible to the generalization effect, and the M3C2 amplitudes grow. However, because they include fewer samples, point clouds generated from subsampled images are more suited for constructing low resolution DTMs for usage in multimedia platforms.

The results obtained from the analysis of the d_{3_4} values shown in Table 4 are given below.

(a) 24.11% of Sample# values are less than 0.20 m. This sort of data has been observed on surfaces that are somewhat distant from the flight plane.
(b) 21.11% of Sample# values are less than 0.40 m. Relevant Sample# values are rarely observed in flat areas. Only the 45.22% of M3C2 values of d_{3_4} are less than 0.40 m.
(c) 20.25% of Sample# values are less than 0.60 m. Relevant Sample# values are intensively observed in flat areas.
(d) 14.10% of Sample# values are less than 0.80 m. Relevant Sample# values are intensively observed in flat areas.
(e) 5.37% of Sample# values are less than 1.00 m. Relevant data were observed in densely all shadowed zones.
(f) 15.05% of Sample# values are greater than 1.00 m. Relevant Sample# values are observed as impulse noise all over the Test Field.

The spatial distribution of the absolute values of Sample# have been illustrated in Fig.s 8-13.

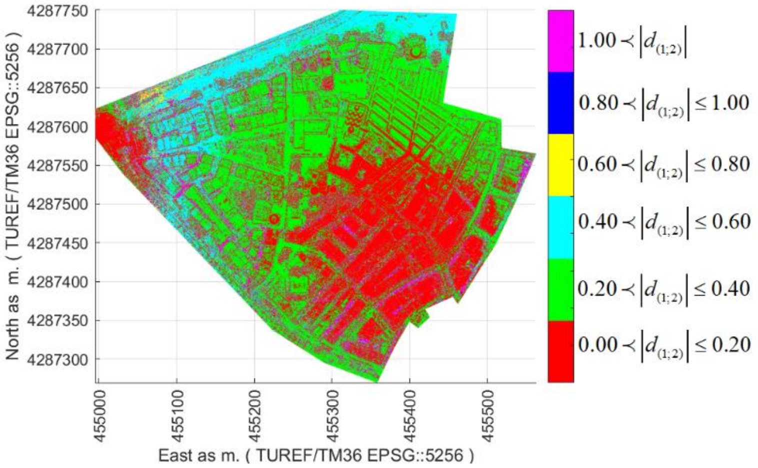

Figure 8 : Spatial distribution of $|d_{(1;2)}|$ values.

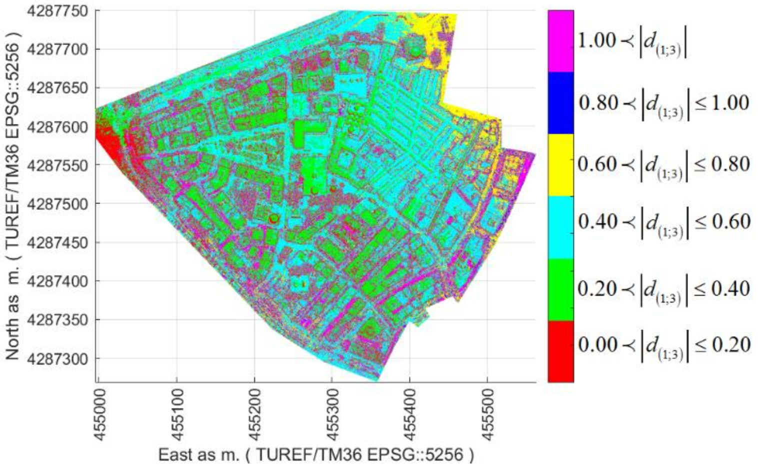

Figure 9 : Spatial distribution of $|d_{(1;3)}|$ values.

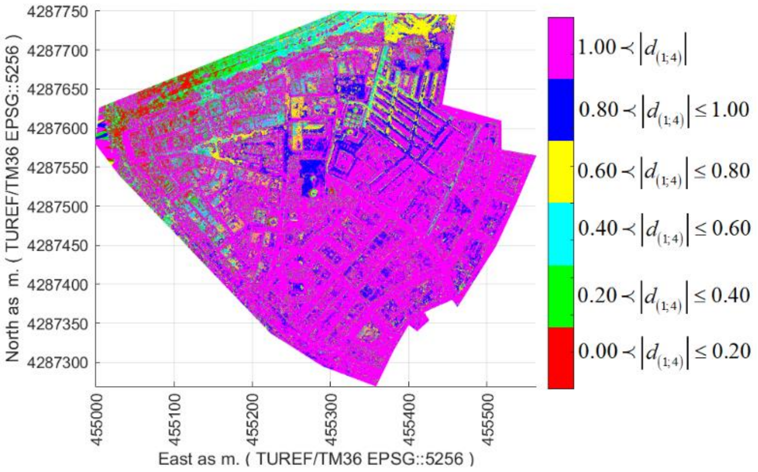

Figure 10 : Spatial distribution of $|d_{(1;4)}|$ values.

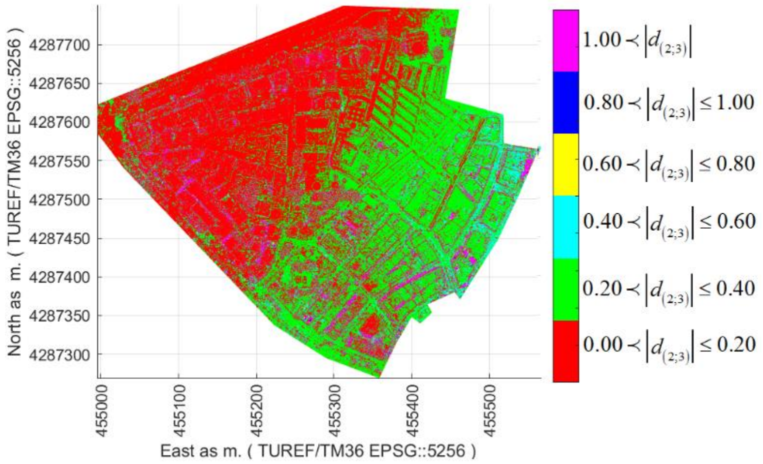

Figure 11 : Spatial distribution of $\left|d_{(2;3)}\right|$ values.

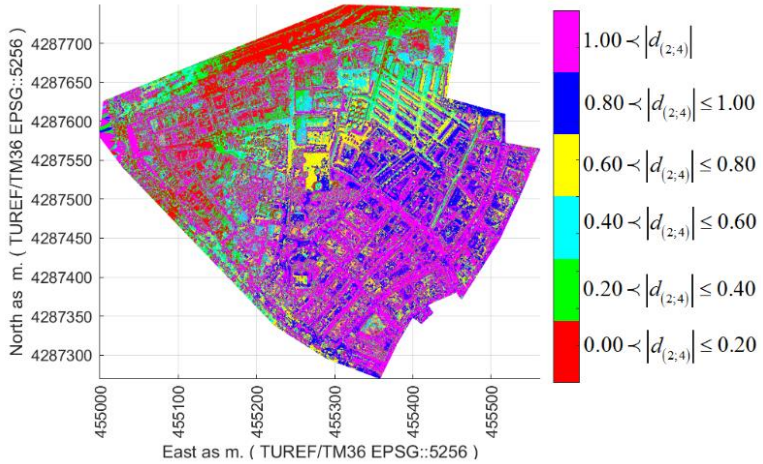

Figure 12 : Spatial distribution of $\left|d_{(2;4)}\right|$ values.

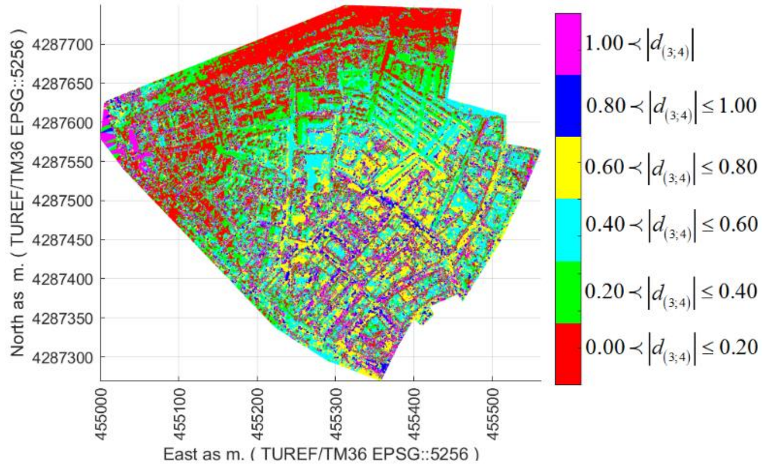

Figure 13 : Spatial distribution of $\left|d_{(3;4)}\right|$ values.

Computational *run-times* of the $Data\#1$, $Data\#2$, $Data\#3$, and $Data\#4$ are captured as 20990.30, 6475.39, 2147.44 and 655.94 in seconds. Run-time complexity varied according to size of processed images in pixels. Therefore, image downsampling reduces data processing time directly.

5. Results and Conclusions

The relationship between image resolution and the level of detail information communicated by a point cloud created through photogrammetry has been carefully examined in this paper. High resolution images can be used to reduce the amount of information lost in the resulting point cloud and orthophoto in applications that call for high resolution spatial data. Low-resolution images make it easier to create surfaces with the right spatial resolution for multimedia applications like augmented reality and virtual reality for mobile platforms and virtual geo-guides. Smoothing high frequency data is necessary to eliminate artifacts caused by artificial noise while downsampling images. This paper introduces a novel method to preserving detail throughout the image downsampling process. The technique described in this paper is relatively sample to implement, fast and quite accurate for practical needs in *3D computational vision* applications.

The following are the findings obtained after interpreting the outcomes of the Experiments described in this study.

1. For SfM-based mapping of areas with dense curving surfaces, areas with very significant changes in local slope, and dense and tall trees, relatively high resolution photos should be employed.

2. Using a low image quality is a quick and efficient technique to create a multiscale DTM. The associated downsampling ratio can be used to regulate the spatial data generalization capacity of the produced multiscale DTMs.

3. As the image resolution declines, the generalization of the surface indicated by the point cloud grows and the detail diminishes.

4. Computations for 3D Mesh generation are performed more quickly on low-dense point clouds. Therefore, low-dense point clouds can be generated by using over downsampled images in SfM photogrammetry.

5. Low-density point clouds enable computations for 3D mesh generation to be completed more quickly. As a result, in SfM photogrammetry, low-dense point clouds can be produced by layering over downsampled images.

6. There is a trade-off between image resolution and smooth rate of 3D mesh surface. Therefore, user must select the image downsampling rate according to accuracy needs of application on the hand.

References

[1] Westoby, M.J., Brasington, J., Glasser, N.F., Reynolds, J.M. 2012. ‘Structure-from-Motion’ photogrammetry: A low-cost, effective tool for geoscience applications. Geomorphology, 179: 300-314.

[2] Mancini, F., Dubbini, M., Gattelli, M., et all.2013. Using Unmanned Aerial Vehicles (UAV) for High-Resolution Reconstruction of Topography: The Structure from Motion Approach on Coastal Environments. Remote Sensing. 5, 12, 6880-6898.

[3] Nam, S., H, Ahn. W., et al. 2019. Content-Aware Image Resizing Detection Using Deep Neural Network. 26th IEEE International Conference on Image Processing (ICIP). 106-110.

[4] Liu, C.Y., Chang, C.C., et al. 2019. Image resizing using fuzzy inferences. IET Image Processing, 13, 12, 2058-2066.

[5] Lau, C.P., Yung, C.P., Lui, L.M. 2018. Image Retargeting via Beltrami Representation. IEEE Transactions On Image Processing, 27, 5787-5801.

[6] Xu, H.F., Yu, S.Y., Wang, C. 2017. An adaptive image resizing algorithm in DCT domain. IEICE Transactions On Information And Systems. E90D(8), 1308-1311.

[7] Park, Y.S., Lee, Y.L., Park, H.W. 2004. Image downsampling for interlaced-to-progressive transcoding in discrete cosine transform domain. Optical Engineering. 43, 9, 2100-2104.

[8] Trentacoste, M., Mantiuk, R., Heidrich, W. 2011. Blur-Aware Image Downsampling. Computer Graphics Forum. 30, 2, 573-582.

[9] Wang, Y.F., Wang, L.J., et al. 2018. Information-Compensated Downsampling for Image Super-Resolution. IEEE Signal Processing Letters, 25, 5, 685-689.

[10] Fang, L., Au, O.C., et al. 2012. Antialiasing Filter Design for Subpixel Downsampling via Frequency-Domain Analysis. IEEE Transactions on Image Processing, 21, 3, 1391-1405.

[11] Huang, F., Yang, H., Tao, J., et al. 2021. Preliminary study on the automatic parallelism optimization model for image enhancement algorithms based on Intel's (R) Xeon Phi. Concurr Comput Pract Exper. 33, 16, e6260. doi:10.1002/cpe.6260.

[12] Huang, F. 202. Research on the parallelization implementation of multi scale retinex image-enhancement algorithm based a MIC platform. Concurr Comput Pract Exper. 32, 22, e5832. doi:10.1002/cpe.5832.

[13] Lee, J., Sung, S. 2016. Evaluating spatial resolution for quality assurance of UAV images. Spatial Information Research. 24, 2, 141-154.

[14] Park, S., Lee, H., Chon, J. 2019. Sustainable monitoring coverage of unmanned aerial vehicle photogrammetry according to wing type and image resolution. Environmental Pollution. 247, 340-348.

[15] Lee, J., Sung, S. 2016. Evaluating spatial resolution for quality assurance of UAV images. Spatial Information Research. 24, 2, 141-154.

[16] Ajibola, I.I., Mansor, S., Pradhan, B., et al. 2019. Fusion of UAV-based DEMs for vertical component accuracy improvement. Measurement. 147 , 106795.

[17] Nesbit, P.R., Hugenholtz, C.H. 2019. Enhancing UAV-SfM 3D Model Accuracy in High-Relief Landscapes by Incorporating Oblique Images. Remote Sensing. 11, 3, 239. DOI:10.3390/rs11030239.

[18] Akar, A. 2017. Evaluation Of Accuracy of Dems Obtained From UAV-Point Clouds For Different Topographical Areas. International Journal of Engineering and Geosciences. 2 , 3, 110-117.

[19] Tomastik, J., Mokros, M. 2017. Accuracy of Photogrammetric UAV-Based Point Clouds under Conditions of Partially-Open Forest Canopy. Forests. 8, 5, 151. DOI:10.3390/f8050151.

[20] Hlotov, V., Hunina, A., Siejka, Z. 2017. Accuracy Investigation Of Creating Orthophotomaps Based On Images Obtained By Applying Trimble-Ux5 Uav. Reports On Geodesy And Geoinformatics. 103, 1, 106-118.

[21] Kucharczyk, M., Hugenholtz, C.H., Zou, X.Y. 2018. UAV-LiDAR accuracy in vegetated terrain. Journal Of Unmanned Vehicle Systems. 6, 4, 212-234.

[22] Cawood, A.J., Bond, C.E., et al. 2017. LiDAR, UAV or compass-clinometer? Accuracy, coverage and the effects on structural models. Journal Of Structural Geology. 98 : 67-82.

[23] Martinez-Carricondo, P., Aguera-Vega, F., et al. 2018. Assessment of UAV-photogrammetric mapping accuracy based on variation of ground control points. International Journal of Applied Earth Observation and Geoinformation. 72 : 1-10.

[24] Jeong, E., Park, J.Y., Hwang, C.S. 2018. Assessment of UAV Photogrammetric Mapping Accuracy in the Beach Environment. Journal Of Coastal Research. 85, 176-180. Doi:10.2112/SI85-036.1.

[25] Uysal, M., Toprak, A.S., Polat, N. 2015. DEM generation with UAV Photogrammetry and accuracy analysis in Sahitler hill. Measurement. 73 :539-543.

[26] Wiseman, DJ and van der Sluijs, J. 2015. Alternative Methods for Developing and Assessing the Accuracy of UAV-Derived DEMs. International Journal Of Applied Geospatial Research. 6 , 3, 58-77.

[27] Cesnulevicius, A., Bautrenas, A., et al. 2019. Comparison of Accuracy of UAV Aerials and Ground Measurements in the Curonian Spit Dunes. Baltic Journal Of Modern Computing. 7 , 4, 571-585.

[28] Huang, F., Lan, B., Tao, J., et al. 2017. A parallel nonlocal means algorithm for remote sensing image denoising on an Intel Xeon Phi platform. IEEE Access. 5 , 8559-8567.

[29] Zhang, X.L., Dai, L.Q. 2019. Fast bilateral filtering. Electronics Letters. 55, 5, 258-259.

[30] Tomastik, J., Mokros, M., et al. 2019. UAV RTK/PPK Method An Optimal Solution for Mapping Inaccessible Forested Areas?. Remote Sensing. 11, 6, 721. DOI10.3390/rs11060721.

[31] Turner, D., Lucieer, A., Wallace, L. 2014. Direct Georeferencing of Ultrahigh-Resolution UAV Imagery. IEEE Transactions On Geoscience And Remote Sensing. 52 , 5, 2738-2745.

[32] Ekaso, D., Nex, F., Kerle, N. 2020. Accuracy assessment of real-time kinematics (RTK) measurements on unmanned aerial vehicles (UAV) for direct geo-referencing. Geo-Spatial Information Science. 23 , 2, 165-181.

[33] Stroner, M., Urban, R., Seidl, J., et al. 2021. Photogrammetry Using UAV-Mounted GNSS RTK: Georeferencing Strategies without GCPs. Remote Sensing. 13, 7, 1336. DOI10.3390/rs13071336.

[34] Forlani, G., Dall'Asta, E., et al. 2018. Quality Assessment of DSMs Produced from UAV Flights Georeferenced with On-Board RTK Positioning. Remote Sensing. 10, 2, 311. DOI10.3390/rs10020311.

[35] Chen, B.H., Tseng, Y.S., Yin, J.L. 2020. Gaussian - Adaptive Bilateral Filter. IEEE Signal Processing Letters. 27, 1670 -1674.

[36] Das, S., Mullick, S.S., Suganthan, P.N. 2016. Recent advances in differential evolution - An updated survey. Swarm And Evolutionary Computation. 27 : 1-30.

[37] Yeo, C.H., Tan, H.L., Tan, Y.H. 2013. On Rate Distortion Optimization Using SSIM. IEEE Transactions on Circuits And Systems For Video Technology. 23 , 7, 1170-1181.

[38] Rukundo, O., Schmidt, S.E. 2018. Effects of rescaling bilinear interpolant on image interpolation quality. Optoelectronic Imaging And Multimedia Technology V. Proceedings of SPIE. 10817. UNSP 1081715. DOI:10.1117/12.2501549.

[39] Jini, P., Kumar, K.R. 2021. Image Inpainting Using Image Interpolation - An Analysis. Revista Geintec-Gestao Inovacao E Tecnologias. 11 ,2, 1906-1920.

[40] Zhang, L.Z., Zhang, W., et al. 2021. Feature-level interpolation-based GAN for image super-resolution. Personal And Ubiquitous Computing. Early Access. DOI:10.1007/s00779-020-01488-y.

[41] Jin, J.G. 2020. An Adaptive Image Scaling Algorithm Based On Continuous Fraction Interpolation And Multi-Resolution Hierarchy Processing. Fractals-Complex Geometry Patterns And Scaling In Nature And Society. 28, 8, 2040016, DOI:10.1142/S0218348X20400162.

[42] Wang, P., Yao, H.Y., Zhang, G. 2021. A novel interpolation-based subpixel mapping for hyperspectral image by using pansharpening. Journal Of Infrared And Millimeter Waves. 40, 1, 56-63.

[43] Won, C.S., Jung, S.W. 2017. Near-reversible efficient image resizing for devices supporting different spatial resolutions. Journal Of Supercomputing. 73, 7, 3021-3037.

[44] Arar, M., Danon, D., Cohen-Or, D., Shamir, A. 2021. Image resizing by reconstruction from deep features. Computational Visual Media. 7 , 4, 453-466.

[45] Yan, B., Tan, W.M., et al. 2017. Codebook Guided Feature-Preserving for Recognition-Oriented Image Retargeting. IEEE Transactions on Image Processing. 26, 5, 2454-2465.

[46] Khan, M.U., Baig, M.A., Moinuddin, A.A. 2017. Full Reference Quality Assessment of Downsized Images. International Conference on Multimedia, Signal Processing and Communication Technologies (Impact). 271-274.

[47] Wang, Q., Yuan, Y. 2014. High quality image resizing. Neurocomputing. 131: 348-356.

[48] Danon, D., Arar, M., et al. 2021. Image resizing by reconstruction from deep features. Computational Visual Media. 7, 4, 453-466.

[49] Trajkovski, K.K., Grigillo, D., Petrovic, D. 2020. Optimization of UAV Flight Missions in Steep Terrain. Remote Sensing. 12, 8, Article Number 1293 .

[50] Sadeq H. A. 2019. Accuracy assessment using different UAV image overlaps. Journal Of Unmanned Vehicle Systems. 7, 3, 175-193.

[51] Torres-Sanchez, J., Lopez-Granados, F., et al. 2018. Assessing UAV-collected image overlap influence on computation time and digital surface model accuracy in olive orchards. Precision Agriculture. 19, 1, 115-133.

[52] Meshroom Software . https://github.com/alicevision/meshroom (last access 30.11.2021)

[53] DiFrancesco, P.M., Bonneau, D., Hutchinson, D.J. 2020. The Implications of M3C2 Projection Diameter on 3D Semi-Automated Rockfall Extraction from Sequential Terrestrial Laser Scanning Point Clouds. Remote Sensing. 12, 11 , Article Number 1885.

[54] CloudCompare Software . https://www.danielgm.net/cc/ (last access 30.11.2021)

[55] Jimenez-Jimenez, S.I., Ojeda-Bustamante, W., et al. 2021. Digital Terrain Models Generated with Low-Cost UAV Photogrammetry: Methodology and Accuracy. ISPRS International Journal Of Geo-Information. 10, 5, 285, DOI: 10.3390/ijgi10050285.

[56] Ferrer-Gonzalez, E., Aguera-Vega, F., et al. 2020. UAV Photogrammetry Accuracy Assessment for Corridor Mapping Based on the Number and Distribution of Ground Control Points. Remote Sensing. 12 , 15 , 2447.DOI10.3390/rs12152447.

[57] RTKLIB Software. http://www.rtklib.com/ (last access 30.11.2021)

[58] UBLOX GNSS Sensors. https://www.u-blox.com/en (last access 30.11.2021)